Robust Analysis of $4e^-$ vs $6e^-$ reduction of Nitrogen on metal surfaces and single atom alloys

Lydia Maria Tsiverioti, Lance Kavalsky, and Venkatasubramanian Viswanathan*

Department of Mechanical Engineering, Carnegie Mellon University, Pittsburgh, Pennsylvania 15213, USA

E-mail: venkvis@cmu.edu

Abstract

The electrochemical synthesis of hydrazine is an exciting avenue in the sustainable production of commonly used chemicals. Taking inspiration from the mechanistic selectivity of reactions such as $2e^-$ vs $4e^-$ ORR, we explore how to fine tune catalysts for hydrazine synthesis through the $4e^-$ electrochemical nitrogen reduction reaction (NRR) over the popular $6e^-$ (NRR) used for ammonia synthesis. Optimal $4e^-$ NRR performance requires sufficient activity as well as selectivity over $6e^-$ (NRR), other mechanistic NRR reaction branching points and the hydrogen evolution reaction. In this study, we perform first principles calculations in conjunction with uncertainty quantification on various monometallic and single atom alloy surfaces to study activity and selectivity of $4e^-$ NRR. Through free energy diagrams, estimation of scaling relations and a theoretical activity volcano, we observe that catalysts exhibiting low activity due to weak binding for NH_3, favor hydrazine synthesis. We also find that single atom alloys follow the same scaling relations as monometallic surfaces. Through uncertainty quantification, we form distributions of limiting potentials and establish a correlation between the activity of a catalyst with the skewness of its limiting potential distribution. We further quantify first principles calculations uncertainty for

branching points within various 4e$^-$ NRR branching points. Reaction branching point analysis and the tradeoff between activity and selectivity of the catalysts points to the significant challenges of pushing NRR towards hydrazine synthesis.

Introduction

The excessive use of fossil fuels and the ensuing environmental crisis are problems that require innovative and sustainable solutions to producing energy and commonly used chemicals.[1] Electrochemical trransformations offer an approach to addressing this challenge.[2–4] Attaining the required activity and selectivity represents a key challenge for the next-generation of electrochemical synthesis.[5] For instance, various scientific studies aim at searching for catalysts selective towards the $2e^-$ oxygen reduction reaction (ORR)[6–9] for hydrogen peroxide synthesis over $4e^-$ ORR, 2e$^-$ oxygen evolution towards hydrogen peroxide over water. Inspired by this approach, we explore selectivity of the $4e^-$ electrochemical Nitrogen reduction reaction (NRR) for hydrazine (NH_2NH_2) synthesis over the $6e^-$ NRR for ammonia (NH_3) synthesis.

$6e^-$ NRR offers a sustainable alternative to the energy intensive Haber-Bosch process, which accounts for 1.44% of global CO_2 emissions.[2] It utilizes an electrochemical cell powered by renewable energy and water/organic additives as a hydrogen atom source.[10] Its $6e^-$ transfer steps and can commence through several reaction pathways. The associative alternating pathway is one of them, and includes hydrazine (NH_2NH_2) as an intermediate after $4e^-$ transfer steps. Hydrazine is traditionally used as rocket fuel because of its high heat of combustion[11] and recent studies have focused on developing direct hydrazine fuel cells (DHFCs).[12–14] Most hydrazine production follows a variation of the the energy intensive Raschig process[11] which involves oxidation of ammonia. Therefore, at present, hydrazine synthesis is heavily dependent on the Haber Bosch process. It is both technologically and scientifically important to explore catalysts that are potentially selective towards hydrazine and the $4e^-$ NRR reaction.

Optimization of either $4e^-$ or $6e^-$ NRR faces several overlapping challenges. The energy associated with adsorbed intermediates in each case scale approximately linearly to each other and consequently, there is a limit to the maximum achievable activity.[15,16] The focus of various theoretical heterogeneous catalysis studies have been to circumvent scaling relations through new classes of materials such as single atom alloys[17] which we will address in more depth. In tailoring systems, we need a better understanding of the uncertainty associated with potential reaction branching points within NRR.[18] More specifically, the $6e^-$ transfer steps bring forth various mechanisms (dissociative, associative alternating/distal, enzymatic) that present a diverse set of intermediates. Gaining confidence on the reaction mechanism is necessary for optimal catalyst selection. This issue is even more pertinent to $4e^-$ NRR; hydrazine is an intermediate only in the associative alternating case. Therefore, it is important to quantify uncertainty at branching points for different pathways and search for a catalyst that is selective towards the associative alternating pathway accordingly. Additionally, $6e^-/4e^-$ NRR competes with the kinetically preferred $2e^-$ hydrogen evolution reaction (HER) reaction; strategies to suppress it are currently quite limited[19] . Future catalysts need to maximize NH_2NH_2/NH_3 yield while minimizing H_2 yield.

Single atom alloys (SAAs) show promise in addressing challenges in various heterogeneous catalysis reactions, such as NRR,[20] CO oxidation,[21] the partial oxidation of methane[22] and the hydrogenation of nitriles.[23] SAAs typically consist of dispersed catalytically active metal atoms X alloyed into a less active host metal Y,[24] which we will denote as Y_1X. Their novel electronic structure and multiple different binding sites display enhanced catalytic activity.[24,25] Kitchin et al.[26] screened 15 SAAs and observed sharp d-orbital features of the single atom near the Fermi edge, similar to the d states in gas phase. They concluded that the d-band center,[27] which usually serves as a robust catalytic descriptor in bulk surfaces, does not accurately capture bonding between the SAA with the adsorbate. Therefore, SAAs broaden

the catalyst search space and could offer ways to deviate from the linear scaling relations of their bulk counterparts. Furthermore, several experimental studies have synthesized a variety of SAAs (Pt_1Cu,[28,29] , Pt_1Au,[30] Pt_1Ag,[31] Ti_1Cu[32]) for hydrogenation reactions and note enhanced selectivity due to unique structural and alloy-bonding properties.[30] Recently, Zheng et al.[20] performed a high throughput screening of transition-metal-doped Au-based SAAs for $6e^-$ NRR and found that several of them (Mo, Ru, Ta, and W) show promising results in terms of stability and selectivity against HER. Inspired by these approaches, we study selectivity between $4e^-$ and $6e^-$ NRR on Au supported SAAs via density functional theory (DFT) calculations.

Quantifying uncertainty in exchange-correlation (XC) functional within DFT is particularly important as it can influence predicted catalyst performance within a given design-space.[33] The Bayesian error estimation functionals-van der Waals (BEEF-vdW) employs bayesian statistics to output an ensemble of functionals that reproduce known DFT errors related to the system of interest.[34] Several studies on $6e^-$ NRR, employ Bayesian error estimation functionals-van der Waals (BEEF-vdW)[34] to build a framework for theoretical uncertainty quantification on common catalytic descriptors successfully.[35,36] Other studies on catalysis have successfully employed BEEF-vdW to quantify DFT errors within hydrogenation of acetylene and 1,3-butadiene,[33] propane dehydrogenation[37] and oxygen reduction.[38] In summary, BEEF-vdW energy ensemble analysis provides confidence in precision of DFT calculations and is leveraged here to make the catalyst search more robust.

In this study, we investigate a variety of monometallic systems and single atom alloys (SAAs) with a Au(111) host to explore their prospects of N_2H_4 synthesis. Specifically, we analyze the free energy diagrams of $4e^-$ and $6e^-$ NRR on each of the systems. Moreover scaling relations of reaction intermediate energies are probed to build an activity volcano and assess catalytic activity and selectivity. We additionally employ BEEF-vdW energy ensemble

analysis to quantify the uncertainty in branching points of $4e^-$ NRR and examine the distributions potential determining steps (PDS). We note the relation between skewness of the PDS distributions and position of the subsequent catalyst on our volcano plot. This observation points to skewness of a PDS distribution as a potential catalytic descriptor and a way to assess how close a catalyst is to the theoretical maximum achievable activity. Branching point analysis indicates the difficulty in optimizing for hydrazine selectivity. Strong binding catalysts donate greater charge than weak binding catalysts and cause N-N bond breakage in an adsorbed hydrazine molecule. On the other hand, weak binding catalysts exhibit low activity and greater selectivity towards HER.

Methodology

Computational Parameters

We simulate our structures with the DFT software GPAW[39] using the Atomic Simulation Environment[40] package. We carry out all calculations using the BEEF-vdW XC and treat ion-electron interactions using the Projected Augmented Wave[41] approach. We employ a grid spacing of 0.18 Å, a $4 \times 4 \times 1$ Monkhorst–Pack k-mesh and we introduce a vacuum spacing of 20 Å. Adsorbates and the top two metal layers were geometrically relaxed until a force convergence of 0.05 eV/Å is reached. Calculations on the (111) facet of the face-centered cubic systems and calculations on the (110) facet of body-centered systems are both performed using $3 \times 3 \times 4$ slabs. We apply Fermi smearing, with a width of 0.05 eV, to enhance convergence. In our calculations we do not account for water layer stabilization, electric field effects and adsorbate coverage effects.

Uncertainty Quantification framework

Current DFT methods require the approximation of the XC functional which introduces uncertainty in the predictions through this choice of model selection. The most commonly

used XC functionals exhibit different strengths and weaknesses associated with complexity and computational cost,[34] however at present there is no universally applicable function. For uncertainty quantification of how this choice of approximation effects quantities such as the PDS and branching point adsorption energies, we utilize the energy ensembles generated by BEEF-vdW.[34] BEEF-vdW consists of a linear combination of GGA exchange energy, PBE[42] and LDA[43] correlation, and a vdW-DF2[44] nonlocal correlation (equation 1). The optimal parameters were obtained by fitting data of intramolecular and intermolecular energetics, bulk solid, and surface chemical bonding.[34] In this study, we employ an ensemble of 2000 XC functionals sampled from this distribution to output total energies. It is from this ensemble that we can then analyze the sensitivity of the systems to perturbing the XC functional and obtain uncertainty estimates. Accounting for uncertainty in our decision loop offers more robustness in future exploration decisions.

$$\mathrm{E_{xc}} = \sum_{\mathrm{m=0}}^{\mathrm{M_x-1}} \alpha_{\mathrm{m}} \mathrm{E_m}^{\mathrm{GGA-x}} + \alpha_{\mathrm{c}} \mathrm{E}^{\mathrm{LDA-c}} + (1-\alpha_{\mathrm{c}}) \mathrm{E}^{\mathrm{PBE-c}} + \mathrm{E}^{\mathrm{nl-c}} \tag{1}$$

Proposed Reaction Mechanism for Electrochemical Hydrazine synthesis

The overall reaction mechanism of hydrazine synthesis consists of a $4e^-$ nitrogen reduction process (reaction 2a) and the overall reaction mechanism for ammonia synthesis consists of a $6e^-$ nitrogen reduction process (reaction 2b)

$$\mathrm{N_2} + 4(\mathrm{H^+} + e^-) \rightarrow \mathrm{N_2H_4} \tag{2a}$$

$$\mathrm{N_2} + 6(\mathrm{H^+} + e^-) \rightarrow 2\mathrm{NH_3} \tag{2b}$$

The associative NRR reaction mechanism consists of nitrogen molecules being adsorbed and breaking after a certain amount of hydrogenation steps. We list all individual steps in reac-

tions 3-8. A branching point in the reaction schemes occurs by forming either NHNH* and NNH_2* from NNH* (steps 4a and 4b). Associative alternating NRR involves the release of an ammonia molecule after the third and sixth hydrogenation steps (reactions 4a, 5a, 6a, 7a, 8) whereas in the associative distal NRR, an ammonia molecules is released during the fifth and sixth hydrogenation steps (reactions 4b, 5b, 6b, 7b, 8). As hydrazine is a reaction intermediate of the associative alternating pathway, its synthesis demands a material that favors this scheme at a preliminary level. We address the uncertainty between intermediates NHNH* and NNH_2* in a later section.

In addition to NHNH* selectivity, an ideal electrocatalyst for hydrazine production must promote hydrazine desorption instead of reaction 8. Therefore, it should not bind strongly to the NH_2* intermediate.

$$N_2 + 6(H^+ + e^-) \rightarrow NNH^* + 5(H^+ + e^-) \tag{3}$$

$$NNH^* + 5(H^+ + e^-) \rightarrow NHNH* + 4(H^+ + e^-) \tag{4a}$$

$$NNH^* + 5(H^+ + e^-) \rightarrow NNH_2* + 4(H^+ + e^-) \tag{4b}$$

$$NHNH^* + 4(H^+ + e^-) \rightarrow NHNH_2^* + 3(H^+ + e^-) \tag{5a}$$

$$NNH_2^* + 4(H^+ + e^-) \rightarrow N^* + NH_3 + 3(H^+ + e^-) \tag{5b}$$

$$NHNH_2^* + 3(H^+ + e^-) \rightarrow NH_2NH_2^* + 2(H^+ + e^-) \tag{6a}$$

$$N^* + 3(H^+ + e^-) \rightarrow NH^* + 2(H^+ + e^-) \tag{6b}$$

$$NH_2NH_2{}^* + 2(H^+ + e^-) \rightarrow NH_2{}^* + (H^+ + e^-) + NH_3 \tag{7a}$$

$$NH^* + 2(H^+ + e^-) \rightarrow NH_2{}^* + (H^+ + e^-) \tag{7b}$$

$$NH_2{}^* + (H^+ + e^-) \rightarrow NH_3 + * \tag{8}$$

Another challenge to synthesizing hydrazine that needs consideration is the suppression of the parasitic hydrogen evolution reaction (HER), which is listed in equations 9a and 9b. More specifically, a good electrocatalyst needs to bind the the NNH^* intermediate more strongly than a proton from the electrolyte.

$$2(H^+ + e^-) + * \rightarrow H^* + (H^+ + e^-) \tag{9a}$$

$$H^* + (H^+ + e^-) \rightarrow H_2 + * \tag{9b}$$

For all adsorption energy calculations the reference is set to gas-phase N_2 and H_2. We employ the computational hydrogen electrode where $\frac{1}{2}\Delta G_{H_2} \rightleftharpoons G_{H^+} + G_{e^-}$ is at equilibrium at a pH of 0. We define the standard free energy at no applied potential (eq. 10a) of an elementary reaction step as the difference between the free energies of the initial and final states. ΔE is the reaction energy of the reactant and product species, ΔZPE is the change in zero point energy and TΔS is the change in entropic contributions. We apply the free gas approximation for entropic contributions of gas molecules and the harmonic approximation for that of adsorbed species at a temperature of 300K. Equation 10b describes the free energy change associated with adsorbants $N_xH_y{}^*$ and products zNH_3/zN_2H_4. The free energy at applied potential U is defined in eq 10c.

$$\Delta G^0 = \Delta E + \Delta ZPE - T\Delta S \tag{10a}$$

$$\Delta G^0{}_{N_xH_y{}^*+zNH_3/zN_2H_4} = G_{N_xH_y{}^*} + zG_{NH_3/N_2H_4} - \frac{x}{2}G_{N_2} - \frac{y}{2}G_{H_2} + G_* \tag{10b}$$

$$\Delta G = neU + \Delta G^0 \tag{10c}$$

Results and discussion

An optimal electrocatalyst for this application promotes hydrazine production and suppresses parasitic competing reactions such as ammonia production and HER. Moreover, this is ideally accomplished at a potential just below the equilibrium potential of U_0= 0.43 V,[5] the maximum potential allowed by thermodynamics based on our calculations. Searching for a candidate system that meets these criteria, we employ a thermodynamic analysis to seek trends that can explain catalytic activity as well as $4e^-$ vs. $6e^-$ N_2 reduction selectivity. As a starting point, we investigate the energetics of each step through free energy diagrams in figure 2a on a variety of simple mono-elemental systems (see free energy diagrams in figure S1 of the SI for all mono elemental systems considered). These landscapes can provide insight into not only predicted activity for a given reaction mechanism, but also selectivity between mechanisms at a given branching point. In terms of the former, this is mainly governed by the PDS, the largest uphill step at U = 0 V in the mechanism, which determines the applied potential necessary to have a downhill landscape. The magnitude of the uphill PDS step should be as small as possible, and identifying this step can lead to design principles moving forward. For all systems apart from V(110), the PDS is the first protonation step, which is a common step to both $4e^-$ and $6e^-$ NRR. Thus, predicted activities for both possible NRR products are coupled, indicating that fine-tuning these systems towards one reaction may also inadvertently influence the other. On V(110) however, the PDS is the fourth protonation step to form adsorbed hydrazine (reaction 6a). While this step does involve the energy

of hydrazine, it is still shared across forming ammonia via the alternating mechanism and also hydrazine synthesis indicating that there could still be coupling. In all cases, we observe that NH_2 adsorbed is more energetically favorable than NH_2NH_2 adsorbed which implies that for all of these systems, a preference towards $6e^-$ NRR may be exhibited. Therefore, decreasing $\Delta G_{NH_2NH_2^*}$-$\Delta G_{NH_2^*+NH_3}$ is an important step towards hydrazine selectivity. Of all of the monometallic surfaces considered, Au(111) exhibits the smallest free energy difference between these two intermediates and merits further investigation.

We further probe the free energy diagrams in figure 2a to examine how intermediate adsorption energies fluctuate relative to each other. In general, scaling between the adsorption energy reaction intermediates is a fundamental roadblock in the NRR design space. Inherent scaling places limits on the minimum overpotential, and thus restricts achievable catalytic activity. At the same time, scaling simplifies search for electrocatalysts, since only one adsorption energy is needed to characterize a whole reaction. The adsorption energies of intermediates on Au(111), Ru(0001) and Pt(111) generally follow similar trends. All three surfaces are less strong binding than V(110) and bond with intermediates via a vertical orientation i.e. through one N atom. We attribute scaling across adsorption energies to the similar nature of the bonding through the single N. V(110) escapes the free energy trends of the later transition metals because it binds reaction intermediates more tightly. Specifically, it forms bonds through both N atoms in N_2H_x radicals in a horizontal orientation and for this reason, presents different scaling. We examine scaling between Au(111), Ru(0001) and Pt(111) in figure 2b; we use NNH^* adsorption energy as the descriptor since it comprises the most uphill step. We are interested in how it scales with adsorption energies that determine selectivity: $\Delta G_{NH_2^*}$ and $\Delta G_{NH_2NH_2^*}$. The BEEF-vdW optimal adsorption energy values give the following scaling relations: $\Delta G_{NH_2^*+NH_3} = 0.82 \times \Delta G_{NNH^*} - 1.16$ and $\Delta G_{NH_2NH_2^*} = 0.28 \times \Delta G_{NNH^*} + 1.31$. In figure 2b we additionally plot the error bars $\pm\sigma_{NH_2^*,NH_2NH_2^*,NNH^*}$, associated with BEEF-vdW generated energy ensembles to underline

the uncertainty associated with DFT generated scaling relations. The intersection between the two lines (when $\Delta G_{NH_2NH_2^*} > \Delta G_{NH_2^*+NH_3}$) defines when ΔG_{NNH^*} is high enough to ensure that NH_3 desorption is less thermodynamically favorable than NH_2NH_2 adsorption at U=0V. This is a necessary but not sufficient condition for hydrazine selectivity. More specifically, as we increase the potential, $\Delta G_{NH_2NH_2^*} - \Delta G_{NH_2^*+NH_3}$ increases. The crossover between the two linear fits occurs at ΔG_{NNH^*}= 4.7 eV which is prohibitively high for NNH^* adsorption. Specifically, even monometallic flat surfaces that display the highest ΔG_{NNH^*} values, i.e. are the most "weak binding", ones such as Au(111) are more than $1eV$ short of the crossover value. Therefore, monometallic surfaces show low selectivity towards $4e^-$ NRR due to their specific scaling. In further exploration of the catalyst space, we need to search for materials that present an intersection point at lower ΔG_{NNH^*} values.

As mentioned earlier, SAAs can potentially exhibit scaling distinct from that of monometallic surfaces due to unique ligand effects and interactions with adsorbates. They combine a strongly binding atom surrounded by a weakly binding host. We observe that Au(111) is the most promising bulk system in terms of selectivity as it exhibits the lowest free energy difference between $NH_2NH_2^*$ and $NH_2^* + NH_3$ (0.90 eV). Thus, we are motivated to explore how selectivity varies if intermediates are adsorbed via a dopant atom embedded at the surface of Au(111). We investigate this design space by performing calculations on the following SAAs: Pd_1Au, Pt_1Au, Ru_1Au, Mo_1Au, Fe_1Au and Re_1Au. Hollow, on top and bridge SAA adsorption types were explored and the on top site of the dopant atom was the most thermodynamically favorable adsorption site for all reaction intermediates. Figure 1 depicts $4e^-$ NRR key reaction intermediates adsorbed on the single atom of a Fe_1Au substrate. In figure 2c we plot the free energies of reaction of intermediates on the SAAs and Au(111) is included for comparison (free energy diagrams of all SAAs considered are included in figure S2 of the appendix). We observe that the PDS for Pt_1Au and Ru_1Au is the first protonation step and for Mo_1Au it is the second protonation step. In all cases,

$NH_2NH_2^*$ is less energetically favorable than $NH_2^* + NH_3$, indicating favoring towards $6e^-$ NRR. The free energy difference between $NH_2NH_2^*$ and $NH_2^* + NH_3$ remains the smallest for Au(111). Therefore, Au(111) displays the highest selectivity for hydrazine in the NH_2 vs NH_2NH_2 branching point relative to the SAAs examined. This accentuates the difficulty in electrochemically synthesizing hydrazine as even the exotic nature of the SAAs could not tune selectivity.

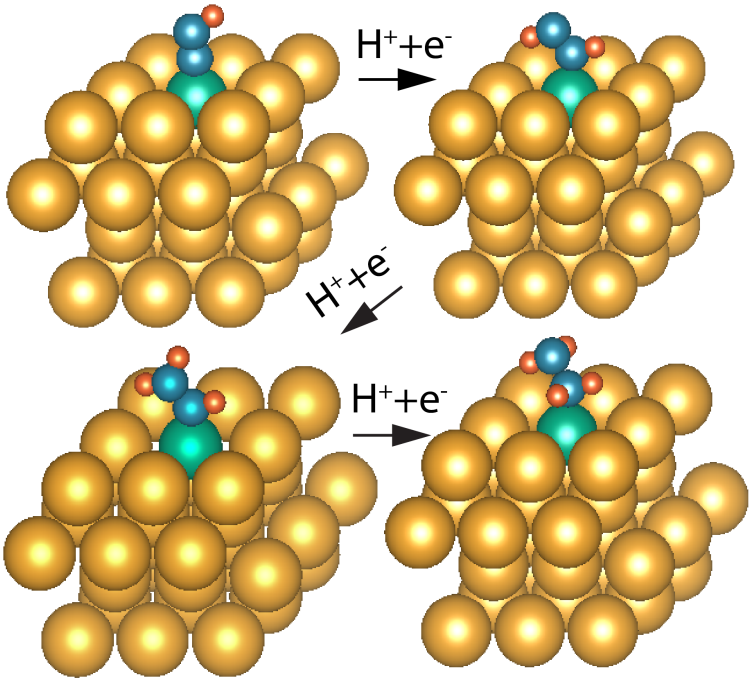

Figure 1: $4e^-$ NRR key reaction intermediates (top to bottom and left to right): NNH^*, $NHNH^*$, $NHNH_2^*$, $NH_2NH_2^*$) adsorbed on Fe atom of a Fe_1Au substrate

To contextualize these findings further, we examine scaling in the SAA cases. Figure 2d, similar to 2b shows the error bars and the scaling relationships between the same reaction intermediates. As seen in figure 2e SAA do not diverge from the scaling of monometallic surfaces. Because of this, we apply the same linear fit to all surfaces. Therefore, the SAAs examined face similar difficulties to monometallic surfaces and present an unfavorable crossover value for hydrazine synthesis.

We construct a theoretical volcano plot (see SI for construction details) in figure 2f to identify the surfaces that approach the underlying activity maximum caused by scaling. Catalysts on the right leg are considered weak binding since they require a relatively uphill step to adsorb reaction intermediate NNH^*, whereas catalysts on the left side more favorably adsorb NNH^* and face a thermodynamic barrier in adsorbing $NHNH_{2*}$. Additionally NH_2 desorption is more thermodynamically challenging for catalysts on the left side than catalysts on the right side. Even though catalysts close to the tip of the volcano, such as Fe(110), Mo_1Au, Ru(0001) show promising activity, they exhibit low hydrazine selectivity since $\Delta G_{NH_2{}^*+NH_3}$ is much lower than $\Delta G_{NH_2NH_2{}^*}$ compared to catalysts on the right. On the other hand, catalysts on the right need to overcome a significant thermodynamic barrier to adsorb NNH^*. This highlights the difficulty in finding a good catalyst for hydrazine selectivity and in the following sections we probe this further via uncertainty quantification.

Potential Determining Step and Limiting Potential (U_L) Uncertainty

We shift our focus to uncertainty quantification of the PDS and limiting potential to gain a more robust understanding of activity and selectivity within our system. A clear understanding of a candidate's limiting potential is paramount for optimizing selectivity. Therefore, the binding energies of adsorbates associated with the PDS determine future design decisions. Doping,[45] applying strain,[46] changing the local coordination environment[47] are examples of tweaking adsorption energies of reaction intermediates to reach desired overpotentials and selectivity. The experiments that stem from these design decisions can be time consuming, so it is important to quantify the uncertainty related with DFT calculated adsorption energies before making them. For instance, Kavalsky et al.[35] explored PDS uncertainty in associative distal $6e^-$ NRR on a $Ru_1/g-C_3N_4$ catalyst and found that two different steps are PDS candidates with 34% and 66% likelihoods. Therefore, one of two steps could be the deciding factor on activity. This accentuates the need to account for precision within DFT

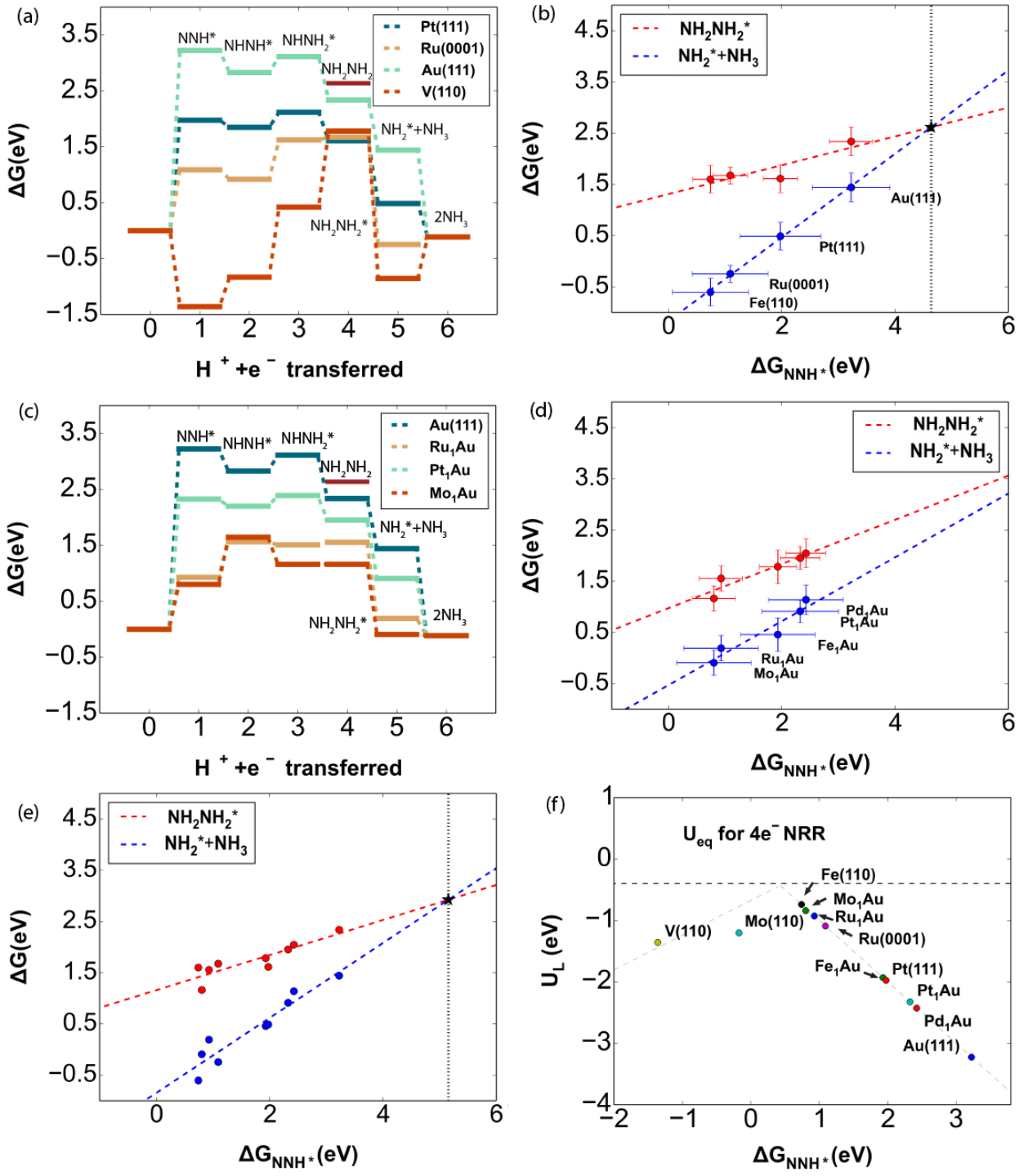

Figure 2: (a) Free energy diagram for 6 e$^-$ NRR for monometallic surfaces Au(111), Ru(0001), Pt(111), V(110) at U=0V, (b) scaling between ΔG_{NNH^*} and $\Delta G_{NH_2NH_2^*/NH_2^*+NH_3}$ with $\pm\sigma_{NH_2^*,NH_2NH_2^*,NNH^*}$ error bars for monometallic surfaces, (c) Free energy diagram for 6 e$^-$ NRR for SAA surfaces Pt_1Au, Ru_1Au, Mo_1Au at U=0V (plotted with Au(111) for comparison), (d) scaling between ΔG_{NNH^*} and $\Delta G_{NH_2NH_2^*/NH_2^*+NH_3}$ with $\pm\sigma_{NH_2^*,NH_2NH_2^*,NNH^*}$ error bars for SAAs, (e) Linear fit (ΔG_{NNH^*} and $\Delta G_{NH_2NH_2^*/NH_2^*+NH_3}$) for both SAAs and monometallic surfaces, (f) theoretical activity volcano for all systems considered

calculations.

Inspired by this approach, we utilize BEEF-vdW generated adsorption energy ensembles to examine PDS uncertainty in $4e^-$ NRR. Specifically, each ensemble member generates its own free energy landscape which in turn gives us a distribution of limiting potentials. We categorize limiting potentials based on reaction steps in figure 3. Weak binding catalysts such as Au(111), Pd_1Au, Pt_1Au and Fe_1Au face a significant thermodynamic barrier to adsorb NNH^* and therefore exhibit 0 % likeliness of having any other elementary step as the PDS. Ru_1Au, Mo(110) and Ru(0001) face less of a barrier to adsorb NNH^* and are closer to the peak of the volcano. Therefore, the PDS shifts towards later protonation steps. Ru_1Au and Ru(0001) are the first catalysts out of the weak binding leg to escape 100% DFT confidence prediction of NNH^* adsorption being the PDS. Ru(0001) exhibits 86% confidence of the first step being the PDS and 13% confidence of the third step being the PDS. Ru_1Au, is closer to the peak of the volcano, and therefore is even less likely to have NNH^* adsorption as the PDS (23%). Conversely, it exhibits 77% confidence that the second step is the PDS (77 %). Mo(110), as the most strong binding catalyst, points to the third(42%), fourth(48%) and sixth(10%) as potential PDS candidates. In all cases, the confidence in DFT prediction of the fifth protonation step as the PDS is uniformly 0 %. As explained earlier, the fifth protonation step needs to be the PDS for $4e^-$ NRR selectivity. Our uncertainty analysis re affirms how challenging it is to stop the reaction at hydrazine adsorption without the subsequent release of an ammonia molecule.

Furthermore, we observe that PDS uncertainty increases as we move towards catalysts near the peak of the volcano. As mentioned above, NNH^* adsorption is a significant thermodynamic barrier for catalysts such as Au(111), Pd_1Au, Pt_1Au and Fe_1Au. This causes the energy ensemble associated with ΔG_{NNH^*} to dominate the distribution of U_L values. However, as we move towards catalysts such as Au_{Ru}, Mo(110) and Ru(0001) different reaction

steps compete to be the PDS. In other words, energy ensembles of different intermediates interact with each other to form the final U_L distribution.

We further utilize BEEF-vdW energy ensembles to extract information on catalytic properties from U_L distributions. In figure 4a we plot the U_L of a variety of catalyst surfaces; as expected, we observe distributions moving to the left as we transition to more strong binding surfaces. We additionally observe that U_L distributions for more strong binding catalysts become narrower. In other words, there is more uncertainty associated with U_L as we move closer to the tip of the activity volcano, but as we noted earlier, there is more uncertainty as to which reaction step causes the U_L. At the same time, stronger binding catalysts exhibit an increasing folding on the left side of their U_L distribution. For instance the U_L distribution of Au(111) has a skewness of 0.025 whereas that of Ru_1Au has a skewness of 0.33. Kavalsky et al. similarly note increasing skewness of U_L distributions as they move to catalysts closer to the tip of their activity volcano. They conclude that the degree of skewness results from the imposed maximum activity of the activity volcano.

We further probe this observation by directly plotting skewness against the U_L values (figure 4b). Ru_1Au is in the upper left corner whereas Au(111) in the lower right corner, and all other catalyst surfaces are in between. This agrees with our activity volcano; as compared to the rest of the catalysts included in the figure 4b, Au(111) has the highest overpotential and Ru_1Au has the lowest. Skewness generally decreases as overpotential increases for Mo(110), Ru(0001), Fe_1Au, Pd_1Au, Pt_1Au. We observe a relatively linear relationship between skewness and limiting potentials as underlined by the linear fit in figure 4b. Generally, we rate the overpotential of a catalyst by where it falls on an activity volcano. This requires performing calculations on several other catalysts to eventually form strong and weak binding legs. Using skewness as a descriptor potentially saves significant time in terms of computations. Skewness, on its own, describes how much a U_L distribution is "pushed back" by the

theoretical minimum achievable overpotential. Therefore, without knowing where the legs of the volcano are, we can still gain insight into how close our catalyst is to the peak of the volcano from looking at that single distribution alone. As a finding, this accentuates how uncertainty quantification can accelerate search for better catalysts in NRR.

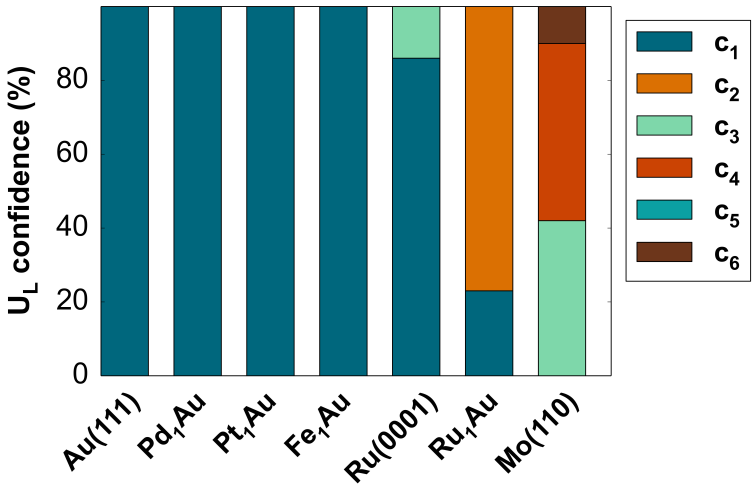

Figure 3: c_i = DFT related certainty that the ith step is the PDS for a given system

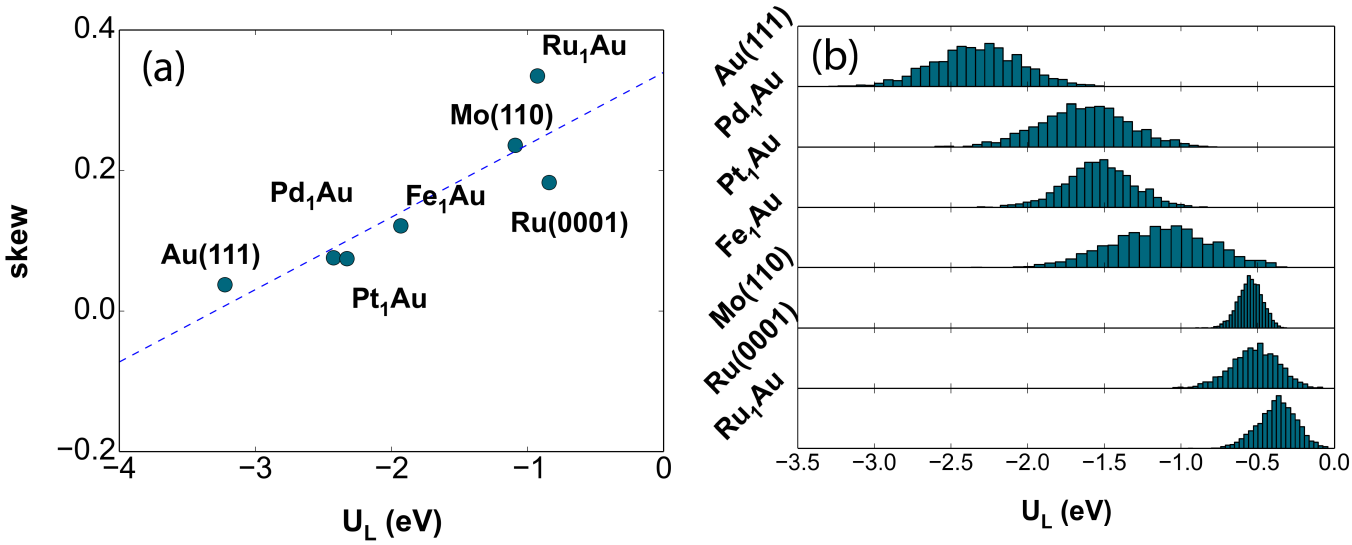

Figure 4: (a) skewness of BEEF-vdW generated UL distributions vs optimal BEEF-vdW UL for a variety of monometallic/SAA surfaces. Individual points reveal a generally linear relationship between the two variables, as indicated by the linear fit, (b) UL distributions for a variety of monometallic/SAA surfaces; as we go down, distributions are "folded" from the right side revealing a theoretical maximum overpotential

Selectivity Uncertainty at 4e$^-$ NRR Branching Points

Activation of N_2 vs H_2

Overcoming the parasitic HER reaction is a major barrier in finding a catalyst for NRR. We attribute this to most of the promising catalysts for NRR simultaneously exhibiting optimal H* binding energies for HER.[15] Therefore, we need to examine whether $\Delta G_{NNH^*} < \Delta G_{H^*}$ is satisfied such that 4e$^-$ NRR can commence. In other words, adsorption and protonation of a nitrogen molecule needs to be more thermodynamically favorable than proton adsorption on the catalyst surface. This is a necessary but not sufficient condition for 4e$^-$ NRR selectivity. NRR needs a less negative overpotential than HER, which means that hydrazine synthesis requires the PDS to be less than the limiting potential for HER ($U_L^{HER} = -\frac{1}{e}\Delta G_{H^*}$).

We visualize ensemble energy distributions for each catalyst on the ΔG_{NNH^*} and ΔG_{H^*} plane (figure 5a, b). The positioning of each catalyst relative to the dashed line ($\Delta G_{NNH^*} = \Delta G^*_{H^*}$)

determines the confidence value, $c_{\text{activation of } N_2 \text{ vs } H_2}$. We define the confidence value in this case as:

$$c_{\text{activation of } N_2 \text{ vs } H_2} = \frac{1}{N_{ens}} \sum_{n=1}^{N_{ens}} \Theta(\Delta G_{NNH^*,n} - \Delta G_{H^*,n}) \tag{11}$$

N_{ens} is the number of XC functionals in the BEEF-vdW ensemble, $\Theta(x)$ is the Heaviside function and $\Delta G_{NNH^*,n}/\Delta G_{H^*,n}$ are reaction free energies for the nth functional. We observe that for the three monoelemental systems considered, Au(111) ($c_{\text{activation of } N_2 \text{ vs } H_2} = 0\%$), Ru(0001) ($c_{\text{activation of } N_2 \text{ vs } H_2} = 0\%$) and Pt(111) ($c_{\text{activation of } N_2 \text{ vs } H_2} = 0\%$) (figure 5a), the functionals uniformly fall on the HER side. This is in alignment with previous findings by Skuylason,[15] and underlines the difficulty of surpassing HER with monoelemental systems. These results indicate that at the first $4e^-$ NRR branching point protons will cover the surface rather than hydrogenate Nitrogen. We do the same for a variety of SAA systems in figure 5b. All SAAs apart from Ru_1Au ($c_{\text{activation of } N_2 \text{ vs } H_2} = 22.75\%$) show a clear preference towards HER. We observe that the positions of ensembles relative to the dashed line follow catalytic trends seen in the activity volcano (figure 2f). Specifically more strong binding systems, which are closer to the tip of the volcano, such as Ru_1Au and Fe_1Au, are closer to the dashed line than catalysts further from the peak such as Au(111) and Pd_1Au. Therefore, catalysts that show high activity for NRR are the most promising candidates to surpass barriers associated with HER. As seen earlier however, weak binding catalysts such as Au(111) exhibit the lowest value. This implies that catalysts that indicate potential for hydrazine selectivity face a significant barrier to overcome HER. This design challenge needs to be addressed in future studies on electrochemical hydrazine synthesis.

Alternating vs Distal Pathway

The branching point at reactions 5b and 5a determines whether the reaction will follow $4e^-/6e^-$ the alternating or $6e^-$ distal NRR pathway. Therefore, from a thermodynamics

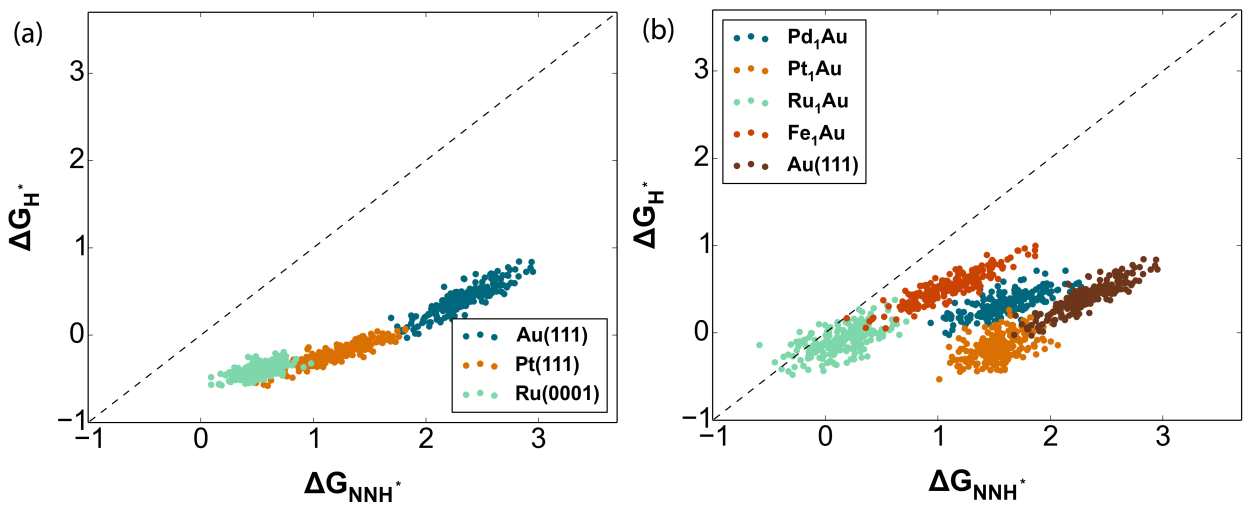

Figure 5: (a) BEEF-vdW generated DFT distributions of a variety of monometallic systems for ΔG_{NNH^*} vs ΔG_{H^*}, (b) BEEF-vdW generated DFT distributions of a variety of SAA systems for ΔG_{NNH^*} vs ΔG_{H^*}, we include Au(111) for comparison

perspective, as the alternating path is necessary to form hydrazine, it is vital to understand how $NHNH^*$ and $NNH_2{}^*$ adsorption energies compare. For instance, if a given catalyst is more selective $NNH_2{}^*$ the reaction will follow a distal mechanism which bypasses hydrazine formation on the way to releasing ammonia. To probe the selectivity at this branch point, we utilize BEEF-vdW generated energy ensembles which allows for a more robust comparison of adsorption energies along with additional insights into their underlying precision.

We utilize a similar approach to the previous section to compare ΔG_{NHNH^*} and $\Delta G_{NNH_2{}^*}$. We project energy ensembles associated with each adsorption energy on the ΔG_{NHNH^*} and $\Delta G_{NNH_2{}^*}$ plane and observe where they fall relative to the dashed line (figure 6a,b). We define the confidence value of an alternating vs distal pathway in this case as:

$$c_{alternating} = \frac{1}{N_{ens}} \sum_{n=1}^{N_{ens}} \Theta(\Delta G_{NHNH^*,n} - \Delta G_{NNH2^*,n}) \tag{12}$$

For Au(111), all functionals prefer an alternating mechanism ($c_{alternating}$=100%). However, ensembles for Pt(111) ($c_{alternating}$=24.25%) and Ru(0001) ($c_{alternating}$=5.25%) exhibit higher bifurcation and a preference towards a distal pathway. In both cases though, the distal

mechanism cannot be completely ruled out. We examine the positions of Au(111), Pt(111) and Ru(0001) on the activity volcano (figure 2f) to see how they relate to NHNH* selectivity. Both Ru(0001) and Pt(111) are considerably closer to the tip of the volcano and stronger binding than Au(111). As we move towards more strong binding catalysts we notice a greater preference towards the distal mechanism. We extend this analysis to SAAs as pictured in figure 6b. Ensembles for Pd_1Au ($c_{alternating}$=100%) and Pd_1Au ($c_{alternating}$=100%) uniformly point towards an alternating pathway, whereas there is higher uncertainty for Ru_1Au ($c_{alternating}$=11.9%) and Fe_1Au ($c_{alternating}$=85.95%). Again, we notice that for more strong binding surfaces (Ru_1Au and Fe_1Au) the adsorption energy ensembles start tilting towards the distal region. Based on the above trends, weak binding surfaces show more promise in surpassing the NHNH* vs NNH_2* selectivity barrier.

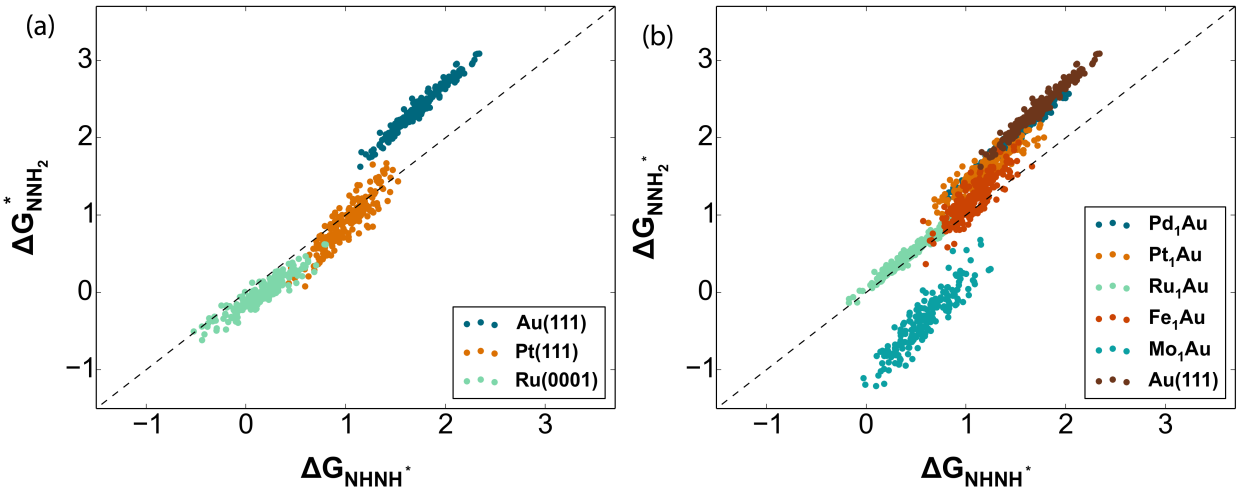

Figure 6: (a) BEEF-vdW generated DFT distributions of a variety of monometallic systems for $\Delta G_{NNH_2^*}$ vs ΔG_{NHNH^*}, (b) BEEF-vdW generated DFT distributions of a variety of SAA systems for $\Delta G_{NNH_2^*}$ vs ΔG_{NHNH^*}, we include Au(111) for comparison

N-N Bond cleavage

To ensure selectivity towards 4e$^-$ NRR over 6e$^-$ NRR we need to enforce at least $\Delta G_{NH_2NH_2^*} < \Delta G_{NH_2^*+NH_3}$ to ensure that NH_2NH_2* adsorption is more thermodynamically favorable than NH_3 desorption at U=0 eV. Higher applied potentials will increase $\Delta G_{NH_2NH_2^*} - \Delta G_{NH_2^*+NH_3}$

because both adsorbates occur at different Proton-coupled electron transfer (PCET) steps. We plot the energy ensembles associated with each adsorption energy on the $\Delta G_{NH_2NH_2^*}$ and $\Delta G_{NH_2^*+NH_3}$ plane and observe where they fall relative to the dashed line (figure 7a,b). We define the confidence value in this case as:

$$c_{NH_2NH_2^*} = \frac{1}{N_{ens}} \sum_{n=1}^{N_{ens}} \Theta(\Delta G_{NH_2NH_2^*,n} - \Delta G_{NH_2^*+NH_3,n}) \tag{13}$$

For mono-elemental systems (figure 7a), we observe that all catalysts almost uniformly favor the PCET from $NH_2NH_2^*$ to $NH_3 + NH_2^*$. Au(111) exhibits slight tilting towards hydrazine adsorption and therefore exhibits superior performance to Ru(0001) and Pt(111) at this branching point. Even though Ru(0001) and Pt(111) are completely above the dashed line, we can still infer catalytic trends based on their relative positioning; Ru(0001) is further away from the dashed line than Pt(111). Therefore, based on the activity volcano (figure 2f), as we move towards more strong binding catalysts in the volcano, energy ensembles move further away from the dashed line.

We extend our analysis to several single atom alloys (figure 7b). Ru_1Au, Mo_1Au and Fe_1Au are uniformly above the dashed line and show 100$ preference towards a fifth PCET step. On the other hand Pd_1Au and Pt_1Au slightly intersect with dashed line. Going back to the activity volcano (figure 2f), we observe a similar relationship to that in mono elemental systems. Specifically, Pd_1Au and Pt_1Au are more weak binding than Ru_1Au, Mo_1Au and Fe_1Au. Therefore, more strong binding catalysts in both bulk and single atom alloys considered show a greater preference towards the release of an ammonia particle. At the same time, weaker binding catalysts, as explained in the previous section, exhibit greater HER affinity. This trade off accentuates the difficulty intrinsic to $4e^-$ NRR selectivity.

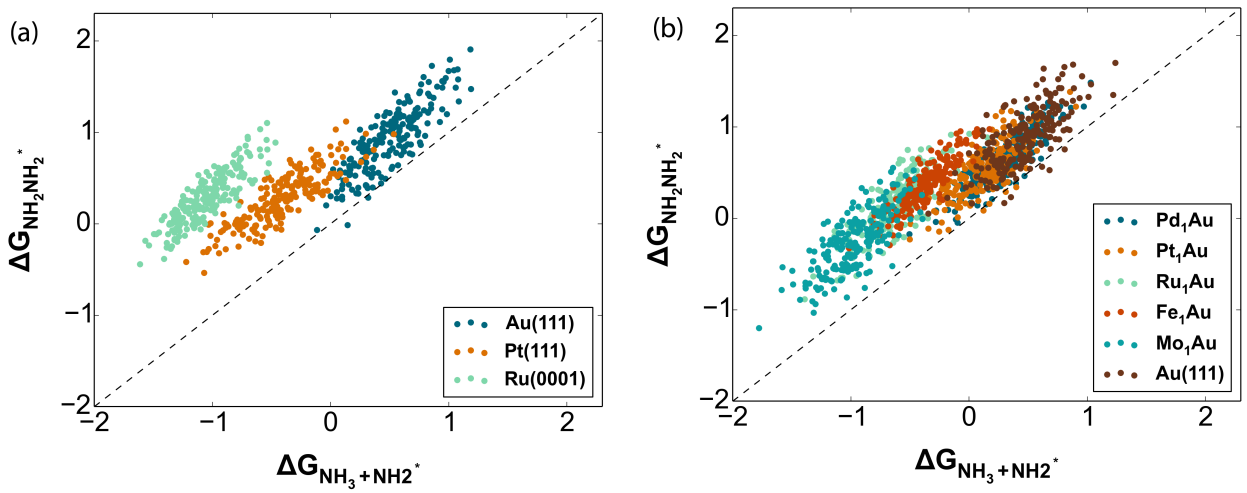

Figure 7: (a) BEEF-vdW generated DFT distributions of a variety of monometallic systems for $\Delta G_{NH_2NH_2^*}$ vs $\Delta G_{NH_2^*+NH_3}$, (b) BEEF-vdW generated DFT distributions of a variety of SAA systems for $\Delta G_{NH_2NH_2^*}$ vs $\Delta G_{NH_2^*+NH_3}$, we include Au(111) for comparison

Conclusion

In this study, we explore selectivity and activity challenges of hydrazine synthesis through $4e^-$ NRR. We perform DFT calculations to find adsorption energies of $4e^-/6e^-$ NRR on a variety of mono-metallic and SAA surfaces and assess $4e^-$ NRR selectivity. Through our activity volcano, we note that catalysts that show high activity suffer from low hydrazine selectivity. In all cases, $6e^-$ NRR is preferred. We utilize BEEF-vdW ensembles to calculate PDS and limiting potential ensembles. We observe that the skewness of the limiting potential distributions indicates how close the catalyst is to the theoretical maximum achievable activity imposed by scaling relations. Using skewness as a descriptor could potentially save computational resources in future catalyst exploration. We additionally use BEEF-vdW energy ensembles to robustly examine how adsorption energies compare at three main branching points of $4e^-$ NRR. For the $NHNH^*$ vs NNH_2^* branching point, we note a preference towards the distal mechanism for more strong binding catalysts and a preference towards the alternating mechanism for weak binding catalysts. At the HER vs $4e^-/6e^-$ NRR branching point, we note a strong preference towards HER for all catalysts. This highlights the difficulty of NRR in general. At the $NH_2NH_2^*$ vs $NH_2 * NH_3$ branching point,

almost all catalysts exhibit a 100% preference towards NH_2^* adsorption. The BEEF-vdW energy ensembles, at this branching point, indicate that more strong binding catalysts are further away from $\Delta G_{NH_2NH_2^*}/\Delta G_{NH_2^*+NH_3}$ intersection. These results highlight the difficulty in catalyzing $4e^-$ NRR, and enforce the need for continuing innovation to facilitate electrochemical synthesis of hydrazine.

Acknowledgement

L.M.T., L.K., and V.V. acknowledge support from the Advanced Research Projects Agency-Energy (ARPA-E), U.S. Department of Energy, under Award Number DE-AR0001211. The views and opinions of authors expressed herein do not necessarily state or reflect those of the United States Government or any agency thereof. L.K. acknowledges the support of the Natural Sciences and Engineering Research Council of Canada (NSERC).

References

(1) Welsby, D.; Price, J.; Pye, S.; Ekins, P. Unextractable fossil fuels in a 1.5 C world. *Nature* **2021**, *597*, 230–234.

(2) Soloveichik, G. Electrochemical synthesis of ammonia as a potential alternative to the Haber–Bosch process. *Nature Catalysis* **2019**, *2*, 377–380.

(3) Ellis, L. D.; Badel, A. F.; Chiang, M. L.; Park, R. J.-Y.; Chiang, Y.-M. Toward electrochemical synthesis of cement—An electrolyzer-based process for decarbonating CaCO3 while producing useful gas streams. *Proceedings of the National Academy of Sciences* **2020**, *117*, 12584–12591.

(4) Perry, S. C.; Pangotra, D.; Vieira, L.; Csepei, L.-I.; Sieber, V.; Wang, L.; Ponce de León, C.; Walsh, F. C. Electrochemical synthesis of hydrogen peroxide from water and oxygen. *Nature Reviews Chemistry* **2019**, *3*, 442–458.

(5) Viswanathan, V.; Hansen, H. A.; Rossmeisl, J.; Nørskov, J. K. Unifying the 2e–and 4e–reduction of oxygen on metal surfaces. *The journal of physical chemistry letters* **2012**, *3*, 2948–2951.

(6) Sun, Y.; Silvioli, L.; Sahraie, N. R.; Ju, W.; Li, J.; Zitolo, A.; Li, S.; Bagger, A.; Arnarson, L.; Wang, X., et al. Activity–selectivity trends in the electrochemical production

of hydrogen peroxide over single-site metal–nitrogen–carbon catalysts. *Journal of the American Chemical Society* **2019**, *141*, 12372–12381.

(7) Melchionna, M.; Fornasiero, P.; Prato, M. The rise of hydrogen peroxide as the main product by metal-free catalysis in oxygen reductions. *Advanced Materials* **2019**, *31*, 1802920.

(8) Viswanathan, V.; Hansen, H. A.; Nørskov, J. K. Selective electrochemical generation of hydrogen peroxide from water oxidation. *The journal of physical chemistry letters* **2015**, *6*, 4224–4228.

(9) Viswanathan, V.; Hansen, H. A.; Rossmeisl, J.; Nørskov, J. K. Universality in oxygen reduction electrocatalysis on metal surfaces. *Acs Catalysis* **2012**, *2*, 1654–1660.

(10) Lee, H. K.; Koh, C. S. L.; Lee, Y. H.; Liu, C.; Phang, I. Y.; Han, X.; Tsung, C.-K.; Ling, X. Y. Favoring the unfavored: selective electrochemical nitrogen fixation using a reticular chemistry approach. *Science advances* **2018**, *4*, eaar3208.

(11) Rothgery, E. F. Hydrazine and its derivatives. *Kirk-Othmer Encyclopedia of Chemical Technology* **2000**,

(12) Serov, A.; Kwak, C. Direct hydrazine fuel cells: A review. *Applied Catalysis B: Environmental* **2010**, *98*, 1–9.

(13) Yamada, K.; Yasuda, K.; Tanaka, H.; Miyazaki, Y.; Kobayashi, T. Effect of anode electrocatalyst for direct hydrazine fuel cell using proton exchange membrane. *Journal of power sources* **2003**, *122*, 132–137.

(14) Yamada, K.; Asazawa, K.; Yasuda, K.; Ioroi, T.; Tanaka, H.; Miyazaki, Y.; Kobayashi, T. Investigation of PEM type direct hydrazine fuel cell. *Journal of power sources* **2003**, *115*, 236–242.

(15) Skulason, E.; Bligaard, T.; Gudmundsdóttir, S.; Studt, F.; Rossmeisl, J.; Abild-Pedersen, F.; Vegge, T.; Jónsson, H.; Nørskov, J. K. A theoretical evaluation of possible transition metal electro-catalysts for N 2 reduction. *Physical Chemistry Chemical Physics* **2012**, *14*, 1235–1245.

(16) Singh, A. R.; Rohr, B. A.; Statt, M. J.; Schwalbe, J. A.; Cargnello, M.; Nørskov, J. K. Strategies toward selective electrochemical ammonia synthesis. *ACS Catalysis* **2019**, *9*, 8316–8324.

(17) Darby, M. T.; Stamatakis, M.; Michaelides, A.; Sykes, E. C. H. Lonely atoms with special gifts: Breaking linear scaling relationships in heterogeneous catalysis with single-atom alloys. *The journal of physical chemistry letters* **2018**, *9*, 5636–5646.

(18) Back, S.; Jung, Y. On the mechanism of electrochemical ammonia synthesis on the Ru catalyst. *Physical Chemistry Chemical Physics* **2016**, *18*, 9161–9166.

(19) Ren, Y.; Yu, C.; Tan, X.; Huang, H.; Wei, Q.; Qiu, J. Strategies to suppress hydrogen evolution for highly selective electrocatalytic nitrogen reduction: challenges and perspectives. *Energy & Environmental Science* **2021**, *14*, 1176–1193.

(20) Zheng, G.; Li, Y.; Qian, X.; Yao, G.; Tian, Z.; Zhang, X.; Chen, L. High-Throughput Screening of a Single-Atom Alloy for Electroreduction of Dinitrogen to Ammonia. *ACS Applied Materials & Interfaces* **2021**, *13*, 16336–16344.

(21) Zhang, Y.; Shi, X.-R.; Sun, C.; Huang, S.; Duan, Z.; Ma, P.; Wang, J. CO oxidation on Ni-based single-atom alloys surfaces. *Molecular Catalysis* **2020**, *495*, 111154.

(22) Meng, Y.; Ding, C.; Gao, X.; Zhang, K.; Wang, J.; Li, Z., et al. Adsorption of Pd on the Cu (1 1 1) surface and its catalysis of methane partial oxidation: A density functional theory study. *Applied Surface Science* **2020**, *513*, 145724.

(23) Wang, H.; Luo, Q.; Liu, W.; Lin, Y.; Guan, Q.; Zheng, X.; Pan, H.; Zhu, J.; Sun, Z.; Wei, S., et al. Quasi Pd 1 Ni single-atom surface alloy catalyst enables hydrogenation of nitriles to secondary amines. *Nature communications* **2019**, *10*, 1–9.

(24) Hannagan, R. T.; Giannakakis, G.; Flytzani-Stephanopoulos, M.; Sykes, E. C. H. Single-atom alloy catalysis. *Chemical Reviews* **2020**, *120*, 12044–12088.

(25) Kyriakou, G.; Boucher, M. B.; Jewell, A. D.; Lewis, E. A.; Lawton, T. J.; Baber, A. E.; Tierney, H. L.; Flytzani-Stephanopoulos, M.; Sykes, E. C. H. Isolated metal atom geometries as a strategy for selective heterogeneous hydrogenations. *Science* **2012**, *335*, 1209–1212.

(26) Thirumalai, H.; Kitchin, J. R. Investigating the reactivity of single atom alloys using density functional theory. *Topics in Catalysis* **2018**, *61*, 462–474.

(27) Nørskov, J. K.; Abild-Pedersen, F.; Studt, F.; Bligaard, T. Density functional theory in surface chemistry and catalysis. *Proceedings of the National Academy of Sciences* **2011**, *108*, 937–943.

(28) Sun, G.; Zhao, Z.-J.; Mu, R.; Zha, S.; Li, L.; Chen, S.; Zang, K.; Luo, J.; Li, Z.; Purdy, S. C., et al. Breaking the scaling relationship via thermally stable Pt/Cu single atom alloys for catalytic dehydrogenation. *Nature communications* **2018**, *9*, 1–9.

(29) Lucci, F. R.; Marcinkowski, M. D.; Lawton, T. J.; Sykes, E. C. H. H2 activation and spillover on catalytically relevant Pt–Cu single atom alloys. *The Journal of Physical Chemistry C* **2015**, *119*, 24351–24357.

(30) Duchesne, P. N.; Li, Z.; Deming, C. P.; Fung, V.; Zhao, X.; Yuan, J.; Regier, T.; Aldalbahi, A.; Almarhoon, Z.; Chen, S., et al. Golden single-atomic-site platinum electrocatalysts. *Nature materials* **2018**, *17*, 1033–1039.

(31) Pei, G. X.; Liu, X. Y.; Wang, A.; Lee, A. F.; Isaacs, M. A.; Li, L.; Pan, X.; Yang, X.; Wang, X.; Tai, Z., et al. Ag alloyed Pd single-atom catalysts for efficient selective hydrogenation of acetylene to ethylene in excess ethylene. *Acs Catalysis* **2015**, *5*, 3717–3725.

(32) Shi, J.; Owen, C. J.; Ngan, H. T.; Qin, S.; Mehar, V.; Sautet, P.; Weaver, J. F. Formation of a Ti–Cu (111) single atom alloy: Structure and CO binding. *The Journal of Chemical Physics* **2021**, *154*, 234703.

(33) Yang, K.; Yang, B. Addressing the uncertainty of DFT-determined hydrogenation mechanisms over coinage metal surfaces. *Faraday Discussions* **2021**, *229*, 50–61.

(34) Wellendorff, J.; Lundgaard, K. T.; Møgelhøj, A.; Petzold, V.; Landis, D. D.; Nørskov, J. K.; Bligaard, T.; Jacobsen, K. W. Density functionals for surface science: Exchange-correlation model development with Bayesian error estimation. *Physical Review B* **2012**, *85*, 235149.

(35) Kavalsky, L.; Viswanathan, V. Robust Active Site Design of Single-Atom Catalysts for Electrochemical Ammonia Synthesis. *The Journal of Physical Chemistry C* **2020**, *124*, 23164–23176.

(36) Medford, A. J.; Wellendorff, J.; Vojvodic, A.; Studt, F.; Abild-Pedersen, F.; Jacobsen, K. W.; Bligaard, T.; Nørskov, J. K. Assessing the reliability of calculated catalytic ammonia synthesis rates. *Science* **2014**, *345*, 197–200.

(37) Zha, S.; Sun, G.; Wu, T.; Zhao, J.; Zhao, Z.-J.; Gong, J. Identification of Pt-based catalysts for propane dehydrogenation via a probability analysis. *Chemical science* **2018**, *9*, 3925–3931.

(38) Vinogradova, O.; Krishnamurthy, D.; Pande, V.; Viswanathan, V. Quantifying confidence in DFT-predicted surface pourbaix diagrams of transition-metal electrode–electrolyte interfaces. *Langmuir* **2018**, *34*, 12259–12269.

(39) Mortensen, J. J.; Hansen, L. B.; Jacobsen, K. W. Real-space grid implementation of the projector augmented wave method. *Physical Review B* **2005**, *71*, 035109.

(40) Larsen, A. H.; Mortensen, J. J.; Blomqvist, J.; Castelli, I. E.; Christensen, R.; Dułak, M.; Friis, J.; Groves, M. N.; Hammer, B.; Hargus, C., et al. The atomic simulation environment—a Python library for working with atoms. *Journal of Physics: Condensed Matter* **2017**, *29*, 273002.

(41) Blöchl, P. E. Projector augmented-wave method. *Physical review B* **1994**, *50*, 17953.

(42) Perdew, J. P.; Burke, K.; Ernzerhof, M. Generalized gradient approximation made simple. *Physical review letters* **1996**, *77*, 3865.

(43) Perdew, J. P.; Wang, Y. Accurate and simple analytic representation of the electron-gas correlation energy. *Physical review B* **1992**, *45*, 13244.

(44) Wellendorff, J.; Bligaard, T. On the importance of gradient-corrected correlation for van der Waals density functionals. *Topics in catalysis* **2011**, *54*, 1143.

(45) Ma, R.; Lin, G.; Zhou, Y.; Liu, Q.; Zhang, T.; Shan, G.; Yang, M.; Wang, J. A review of oxygen reduction mechanisms for metal-free carbon-based electrocatalysts. *npj Computational Materials* **2019**, *5*, 1–15.

(46) Luo, M.; Guo, S. Strain-controlled electrocatalysis on multimetallic nanomaterials. *Nature Reviews Materials* **2017**, *2*, 1–13.

(47) Zhuang, Z.; Kang, Q.; Wang, D.; Li, Y. Single-atom catalysis enables long-life, high-energy lithium-sulfur batteries. *Nano Research* **2020**, *13*, 1856–1866.

TOC Graphic